Evolution of distorted rotating black holes. II. Dynamics and analysis

Steven R. Brandt and Edward Seidel
National Center for Supercomputing Applications, 605 East Springfield Avenue, Champaign, Illinois 61820 and Department of Physics, University of Illinois at Urbana-Champaign, Urbana, Illinois 61801
(Received 19 December 1994)

We have developed a numerical code to study the evolution of distorted, rotating black holes. This code is used to evolve a new family of black hole initial data sets corresponding to distorted "Kerr" holes with a wide range of rotation parameters, and distorted Schwarzschild black holes with odd-parity radiation. Rotating black holes with rotation parameters as high as $a/m = 0.87$ are evolved and analyzed in this paper. The evolutions are generally carried out to about $t = 100M$, where M is the ADM mass. We have extracted both the even- and odd-parity gravitational waveforms, and find the quasinormal modes of the holes to be excited in all cases. We also track the apparent horizons of the black holes and find them to be a useful tool for interpreting the numerical results. We are able to compute the masses of the black holes from the measurements of their apparent horizons, as well as the total energy radiated and find their sum to be in excellent agreement with the ADM mass.

PACS number(s): 04.30.Db, 04.25.Dm, 95.30.Sf, 97.60.Lf

I. INTRODUCTION

In this paper we present the first results for the evolution of initial data sets corresponding to axisymmetric, rotating vacuum black holes. We developed a numerical scheme and code based on an extension of earlier work at NCSA [1–4] on distorted, but nonrotating, axisymmetric black holes. In a companion paper, referred to henceforth as paper I [5], we describe the numerical methods, gauge conditions, and code tests developed for a code to evolve rotating black hole spacetimes. With this new code we have been able to evolve and study a new family of distorted rotating black hole data sets. The construction of these data sets was outlined in paper I, and will be discussed in another paper in this series [6], which we refer to as paper III. In this paper we focus on analyzing the physics of the evolution for a number of different rotating black hole data sets, with both even- and odd-parity radiation. We also consider the evolution of nonrotating black holes that have been distorted by the presence of odd-parity gravitational waves.

These rotating black holes can be highly distorted, allowing one to study their nonlinear dynamics. These studies will be useful not only in understanding rotating black hole spacetimes, but also in studying the late stages of black hole collisions with angular momentum, just after the holes have coalesced. At that time they will have formed a single, highly distorted rotating hole similar to the configurations studied here.

In analyzing these rotating black hole evolutions, we have developed a series of tools that allow us to study gravitational waves, apparent horizons, and other quantities of interest. Using these tools we have extracted the waveforms for both the even- and odd-parity radiation emitted by a distorted rotating black hole, and we find that the quasinormal modes of the hole are excited. The extracted waveforms are also used to compute the energy carried away from the black hole via gravitational waves. We locate and study the geometry of the apparent horizons in these spacetimes, and find that their geometric structure can be used as a key tool in analyzing the evolution. We show how to extract information about the oscillation frequency, the mass, and the angular momentum of the black hole.

The organization of this paper is as follows. In Sec. II we define the variables used in our simulations and describe the variety of initial data sets we evolve and analyze in this paper. In Sec. III we present an analysis of "near zone" results from evolving various initial data sets, including an analysis of the physics that can be extracted from apparent horizons. Section IV contains a discussion of our extraction methods to compute the even- and odd-parity radiation in the spacetime, while Sec. V contains a discussion of the results of evolving the data sets. Finally, in Sec. VI we conclude and discuss future directions this research will take.

II. CODE AND INITIAL DATA

The code we developed to evolve rotating black hole data sets has been discussed in detail in Ref. [5]. We will not discuss any details of the numerical methods used to evolve the spacetimes here, but for context we define our notation for the primary variables used in our code.

A. Definition of variables

We build on earlier work of Ref. [1,4] on nonrotating black holes in defining the variables used in our code. Additional metric and extrinsic curvature variables must be introduced to allow for the odd-parity modes present in this new system. Previously only even-parity modes were present. We define the variables used in our evolutions as

$$\gamma_{ij} = \begin{pmatrix} \gamma_{\eta\eta} & \gamma_{\eta\theta} & \gamma_{\eta\phi} \\ \gamma_{\eta\theta} & \gamma_{\theta\theta} & \gamma_{\theta\phi} \\ \gamma_{\eta\phi} & \gamma_{\theta\phi} & \gamma_{\phi\phi} \end{pmatrix} = \Psi^4 \begin{pmatrix} A & C & E\sin^2\theta \\ C & B & F\sin\theta \\ E\sin^2\theta & F\sin\theta & D\sin^2\theta \end{pmatrix} \tag{1a}$$

and

$$K_{ij} = \Psi^4 h_{ij} = \Psi^4 \begin{pmatrix} H_A & H_C & H_E\sin^2\theta \\ H_C & H_B & H_F\sin\theta \\ H_E\sin^2\theta & H_F\sin\theta & H_D\sin^2\theta \end{pmatrix}. \tag{1b}$$

In these expressions η is a logarithmic radial coordinate, and (θ,ϕ) are the usual angular coordinates. The relation between η and the standard radial coordinates used for Schwarzschild and Kerr black holes is discussed in paper I. As in Ref. [4], the conformal factor Ψ is determined on the initial slice and held fixed in time afterwards. The introduction of Ψ into the extrinsic curvature variables simplifies the evolution equations somewhat. The various factors of $\sin\theta$ are included in the definitions to explicitly account for their behavior near the axis of symmetry and the equator, as discussed in paper I.

B. Initial data

We constructed a new class of initial data sets corresponding to distorted rotating black holes and odd-parity distorted nonrotating black holes. The construction of these data sets is described in paper I and in more detail in paper III. Here we briefly describe the different classes of data sets and describe our parameter choices for evaluation and analysis. There are three basic families of black hole data sets that are evolved and analyzed in this paper. The first series of data sets, labeled in Table I as runs $k1$ and $k2$, correspond to Kerr black holes with rotation parameters $a/m = 0.48$ and 0.68, respectively. As described in paper I, these data sets have been transformed from Boyer-Lindquist coordinates into our logarithmic η coordinates and then evolved.

The second family of initial data sets that we consider are related to the rotating black hole initial data of Bowen and York [7], but we have added a "Brill wave" to distort them with a construction similar to that of Ref. [8]. As described in paper I, the initial three-metric γ_{ab} is chosen to be

$$ds^2 = \Psi^4 \left[e^{2q} \left(d\eta^2 + d\theta^2 \right) + \sin^2\theta \, d\phi^2 \right], \tag{2}$$

where the "Brill wave" function q is given by

$$q = \sin^n\theta \, q_G, \tag{3a}$$

$$q_G = Q_0 \left(e^{-s_+} + e^{-s_-} \right), \tag{3b}$$

$$s_\pm = (\eta \pm \eta_0)^2 / \sigma^2. \tag{3c}$$

The extrinsic curvature is computed following Bowen and York, with a free parameter J that specifies the angular momentum of the hole. For more details of how the constraints are solved, refer to paper I. Here we simply point out that the Bowen-York solution to the momentum constraint is

$$H_E = 3\Psi^{-6} J, \tag{4a}$$

$$H_F = 0. \tag{4b}$$

We note that for $J = 0$, the data sets reduce to the "Brill wave plus black hole" distorted black hole data sets described in Ref. [1], and for the Brill wave parameter $q = 0$ the Bowen-York solutions result.

The initial data sets described in Table II whose name begins with an r ($r0$–$r5$) describe a sequence of distorted rotating holes of increasing rotation. The run $r0$ has no angular momentum, while run $r5$ is a pure Bowen-York black hole without a Brill wave added, but with a significant amount of rotation. As we will see in Sec. III A 3 below, it is rotating so fast ($a/m = 0.87$) that its horizon cannot be completely embedded in three-dimensional Euclidean space, yet we are able to evolve it accurately.

TABLE I. This table gives summary data for evolutions of pure Kerr spacetimes. J is the total angular momentum of the spacetime; a/m is the usual rotation parameter in the Kerr metric.

Case	J	a/m
$k1$	2.5	0.481
$k2$	5.0	0.677

TABLE II. This table gives input parameters for each of the runs. J describes the amount of angular momentum in the system, Q_0 the amplitude of the Brill wave placed in the spacetime, σ gives the width of the Brill wave, η_0 gives the location of the peak of the Brill wave distortion, and the parameter n (n') describes the radial dependence of the distortion in the metric (extrinsic curvature).

Case	J	Q_0	σ	η_0	n	n'
$r0$	0.0	1.0	1.0	1.0	2	NA
$r1$	2.5	1.0	1.0	1.0	2	NA
$r2$	5.0	1.0	1.0	1.0	2	NA
$r3$	10.0	1.0	1.0	1.0	2	NA
$r4$	10.0	0.5	1.0	0.0	2	NA
$r5$	15.0	0.0	NA	NA	NA	NA
$o1$	0.0	2.0	1.0	2.0	NA	3
$o2$	0.0	2.0	1.0	2.0	NA	5

Finally we have considered a third family of distorted black hole data sets that correspond to odd-parity radiation superimposed on nonrotating black holes. In this case the three-metric γ_{ab} is described by the same Brill wave parameters in Eq. (3) above, but the extrinsic curvature is taken to be

$$H_E = \Psi^{-6} q_G \left[(n'+1) - (2+n')\sin^2\theta\right] \sin^{n'-3}\theta, \quad (5a)$$

$$H_F = -\Psi^{-6}\, \partial_\eta q_G \cos\theta \sin^{n'-1}\theta. \quad (5b)$$

The parameter n' is used to describe an "odd-parity" distortion. It must be odd, and have a value of at least 3. This family of data sets does not describe rotating black holes, as discussed in paper I and in more detail in paper III. The two data sets in Table II whose name begins with o ($o1$ and $o2$) represent a family of odd-parity distortions of nonrotating holes. As we will see in Sec. III A 3 below, the angular index n' is related to the dominant ℓ mode in the distortion of these holes. Both an $n'=3$ and an $n'=5$ data set are given because the former emitted virtually all of its radiation in the $\ell=3$ mode and we were also interested in examining significant $\ell=5$ radiation from an odd-parity distortion.

We summarize the dimensionless angular momentum parameter (a/m) of these spacetimes in Table III where three different measurements are tabulated. The meanings of the columns are as follows: $(a/m)_{\rm min} = J/M^2_{\rm ADM}$, and would be the rotation parameter of the system if none of the radiation escapes to infinity. $(a/m)_{\rm max} = J/M^2_{\rm AH}$, where $M_{\rm AH}$ is the mass of the apparent horizon defined by Eq. (10) below, and would be the rotation parameter of the final system if the area of the black hole did not increase at all during the evolution. These two measurements are made on the initial data sets without evolving them. Finally $(a/m)_{\rm cr}$ is the value of (a/m) obtained by measuring the shape of the apparent horizon surface during the evolution as discussed below and in Ref. [9].

TABLE III. This is a table of a/m values calculated from the initial data. $(a/m)_{\rm min} = J/M^2_{\rm ADM}$ on the initial slice and will be the final value if all the energy in the spacetime goes into the horizon, and $(a/m)_{\rm max} = J/M^2_{\rm AH}$ on the initial slice which will be the final value if the surface area of the horizon does not increase during the evolution. The parameter $(a/m)_{\rm cr}$ is the angular momentum extracted from the horizon.

Case	$(a/m)_{\rm min}$	$(a/m)_{\rm max}$	$(a/m)_{\rm cr}$
$r0$	0.000	0.000	0.000
$r1$	0.342	0.600	0.351
$r2$	0.432	0.698	0.436
$r3$	0.511	0.759	0.512
$r4$	0.696	0.827	0.703
$r5$	0.868	0.886	0.870
$k1$	0.480	0.481	0.481
$k2$	0.675	0.677	0.677

III. NEAR ZONE PHYSICS

In this section, we discuss details of the "near zone" evolution of several black holes, focusing on the apparent horizon. We present an apparent horizon finder, and discuss the dynamics of the apparent horizon as a tool to study the physics of the near zone. Although extremely important to the numerical evolution, the behavior of the metric functions themselves generally does not illuminate the physics of the system, and is not discussed here. We refer the interested reader to paper I for discussion of metric evolution.

A. Horizons

In this section we examine the properties of the black hole apparent horizons in the spacetimes evolved here. The apparent horizon is defined as the outermost trapped surface. Because a knowledge of the future is required to identify the event horizon, the concept of an apparent horizon is useful in numerical relativity. The location of the apparent horizon depends only on information known within a given time slice, is always inside the event horizon [10], and coincides with the event horizon in a stationary spacetime. As shown in Ref. [11], where studies of perturbed event and apparent horizons were made, apparent horizons can closely approximate the event horizons even in dynamic spacetimes, and share many dynamical features with them. In this paper we focus on the apparent horizon, but will treat the event horizon of highly distorted black holes in a future work.

Mathematically the apparent horizon condition is expressed by requiring the expansion of all outgoing null normals to the surface to vanish. This condition can be written as [12]

$$D_a s^a + K_{ab} s^a s^b - {\rm tr}K = 0, \quad (6)$$

where s^a is the outward-pointing normal vector to the surface in the three-dimensional subspace. If such a surface exists, it is said to be a marginally trapped surface. In some cases multiple surfaces satisfying this condition can be found, and the outermost one is then defined to be the apparent horizon. The apparent horizon finder searches for a solution to this equation by making an initial guess, and then iteratively solving the above nonlinear equation via the Newton-Raphson method until we obtain the desired accuracy [9].

The initial guess that we use is an η =const surface where the value of η used is the outermost value which satisfies the condition

$$0 = \frac{1}{\Psi^2\sqrt{A}}\left(4\frac{\partial_\eta \Psi}{\Psi} + \frac{\partial_\eta D}{D}\right) - 2\frac{H_D}{D} \quad (7)$$

on the equator ($\theta = \pi/2$). This may be interpreted as the condition that the light rays confined to the equatorial

plane have null expansion. The radius thus determined provides us with a good estimate of the position of the apparent horizon. This technique proved valuable because it made it easier to follow the horizon when it jumped outward from the throat at about $t \approx 10M$. This particular complication is a result of using an antisymmetric lapse that vanishes on the throat of the black hole, preventing evolution there (except through the shift terms). The initial apparent horizon is usually located on the throat (the throat is guaranteed to be a minimal surface, but not necessarily an apparent horizon). With a lapse that vanishes on the throat, the horizon often remains there until some evolution has occurred, at which point it may jump out discontinuously. This technique does not require the horizon position from previous time steps to be recorded, allowing us to find the horizon as infrequently as we wish, or to find it again if it becomes lost. This trick has been quite successful and uses up little CPU time. Once we have located the horizon with this method, it can be analyzed to provide physical information as we describe in the following sections.

1. Masses

In addition to the Arnowitt-Deser-Misner (ADM) mass, which was calculated on the initial slice, we are interested in obtaining a dynamic mass during the evolution. The measure we will use for this is an "areal mass" based on the irreducible mass (as given by the apparent horizon) and the angular momentum of the black hole.

The horizon finder returns the location $\eta(\theta)$ of the apparent horizon on a given slice. In order to study the geometric properties of the horizon, from which important physical information can be obtained, it is useful to determine the two-dimensional submetric induced on the surface by defining a new coordinate ξ by the equation $\eta = \eta(\theta)\xi$. We now have

$$dl^2 = \Psi^4 \left\{ A d\xi^2 + \left[B + A\xi^2 \left(\frac{d\eta}{d\theta}(\theta) \right)^2 \right] d\theta^2 + D d\phi^2 + 2F d\phi d\theta \right\}. \tag{8}$$

The submetric that we are interested in may be found by letting ξ be equal to 1. The surface area of the horizon is, therefore,

$$A = 2\pi \int_0^\pi \sin\theta \Psi^4 d\theta \sqrt{\left[B + A \left(\frac{d\eta}{d\theta}(\theta) \right)^2 \right] D - F^2}. \tag{9}$$

For a Schwarzschild black hole the mass is given by $M_{\rm ir}$ below, and for a Kerr black hole the mass is determined by both the surface area and angular momentum of the hole [13], according to the relationships

$$M_{\rm ir} = \sqrt{\frac{A}{16\pi}} \tag{10a}$$

and

$$M_{\rm AH}^2 = M_{\rm ir}^2 + \frac{J^2}{4M_{\rm ir}^2}. \tag{10b}$$

Although our spacetimes are not stationary and hence the apparent horizon does not coincide exactly with the event horizon, these are quite useful quantities to take for the dynamical mass. The above formulations describe the minimum mass of the final Kerr black hole that is possible at the end of the evolution [14]. However, as shown in Refs. [11,15] the event and apparent horizons are often quite close, even in dynamic spacetimes, and the mass described in Eqs. (10) should often be a good approximation to the event-horizon-based mass. The masses computed in this way will be used extensively in analyzing the evolutions presented in Sec. V below.

2. Oscillations

Once we have the two-metric on the horizon's surface we can measure the horizon geometry. An example of such a measurement is C_r, the ratio of polar circumference (C_p) to the equatorial circumference (C_e) of the apparent horizon. The horizon of a stationary black hole has a characteristic shape that depends upon its rotation parameter a/m [16]. For a stationary or a dynamic black hole, this shape can be used to obtain the rotation parameter, as discussed in Ref. [9]. There it was shown that the horizon oscillates about this equilibrium stationary shape with the quasinormal mode frequencies of the black hole. We can plot the shape parameter C_r as a function of time to measure these horizon dynamics. Here we extend this technique and apply it to new spacetimes not considered in Ref. [9].

To obtain the polar and equatorial circumferences we first transform the two-metric so that it becomes diagonal. This is accomplished by introducing a new coordinate, χ. The metric on the two-surface defined by the apparent horizon now becomes

$$d\chi = d\phi - \frac{F}{D\sin\theta} d\theta, \tag{11a}$$

$$B' = \Psi^4 \left[B + A \left(\frac{\partial\eta}{d\theta}(\theta) \right)^2 + \frac{F^2}{D} \right], \tag{11b}$$

$$F' = 0, \tag{11c}$$

$$D' = \Psi^4 D. \tag{11d}$$

The polar circumference and the equatorial circumfer-

ence may now be defined as

$$C_p = \oint d\theta \sqrt{B'} \tag{12a}$$

and

$$C_e = \oint d\phi \sqrt{D'}. \tag{12b}$$

It was shown in previous work [9] that the $\ell = 2$ and $\ell = 4$ quasinormal mode (QNM) frequencies can be seen in the function C_r, which can also be analyzed to obtain the rotational speed (a/m) of the spacetime. This is accomplished by first fitting C_r to the fundamental $\ell = 2$ QNM, the first overtone $\ell = 2$ QNM, and a constant offset from unity. We assume that the oscillations are dominated by the $\ell = 2$ quasinormal ringing radiation going down the horizon. As discussed in Ref. [9], the ringing radiation is generated at the "peak of the potential barrier" located outside the horizon. Part of this signal propagates away from the hole and part goes down the hole, causing the horizon to oscillate as the signal crosses it. The offset is used in the fit because a rotating black hole will not be spherical (a sphere would have $C_r = 1$) but should be oblate (in equilibrium), producing an "offset" in C_r. The fitted value of the constant offset can then be used to obtain the value of a/m for the surface, since for a Kerr black hole the oblateness is a unique function of the rotation parameter. [We note that the following function is an approximation generally accurate to within 2.5% for a/m as a function of C_r: $a/m = \sqrt{1-(-1.55+2.55C_r)^2}$.] In Table III we show the value of the rotation parameter a/m for the family of data sets labeled $r0$–$r5$ obtained with this method.

Finally, as the horizon oscillations should be caused by radiation from all black hole modes excited during the evolution, not just the $\ell = 2$ modes, one can analyze the function C_r for other modes as well. For example, the fit to the shape parameter in terms of the $\ell = 2$ QNM expansion functions can be subtracted from the actual function C_r, leaving a residual of higher modes. In Ref. [9] we showed how this remaining signal was dominated by $\ell = 4$ QNM's for some spacetimes.

For the odd-parity distorted holes ($o1$ and $o2$, not shown), the oscillations in C_r are second order in the metric perturbation. As a result the spectrum of frequencies in the surface vibrations that result from the $\ell = 2$ and $\ell = 3$ QNM's will be much larger. Therefore the oscillations are more complicated than in the previous cases. Further details of the surface oscillations of these black holes will be given in Sec. III B.

In Fig. 1 we plot C_r as a function of time for simulation $r4$. This is a distorted Bowen-York hole rotating quite rapidly. The solid line shows the value of C_r extracted from the horizon. The dashed line shows the fit to the two lowest $\ell = 2$ QNM's, and the straight horizontal dashed line shows the constant offset that came from the fit. Note that the fit matches the oscillation quite well except at very late times, when we expect the code to be less accurate, particularly near the horizon where metric functions tend to develop steep gradients [17]. This

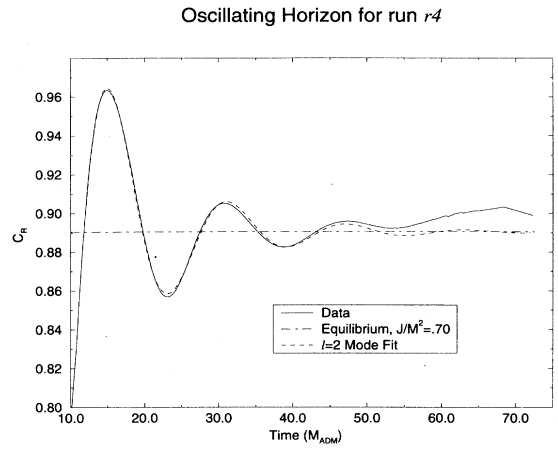

FIG. 1. In this figure we plot the function C_r (the ratio of polar to equatorial circumference of the apparent horizon) as computed by our code for run labeled $r4$, a distorted rotating black hole. We have removed the early part of this plot where the horizon "jumps out" so that we can more clearly see the surface oscillations. The line labeled "equilibrium" is the offset from sphericity determined by our fit. This offset implies that the system is oscillating about an "equilibrium" Kerr black hole with a rotation parameter of $a/m = 0.70$.

analysis shows that the black hole is oscillating about a Kerr black hole with a rotation parameter of $a/m = 0.70$, consistent with estimates made on the initial slice.

Figure 2 shows a similar plot for the function C_r and its fit for run $r5$. Run $r5$ differs from runs $r0$–$r4$ in that $r5$ is a pure Bowen-York black hole. It is thus much more noticeably oblate, with $C_r \approx 0.81$, as opposed to

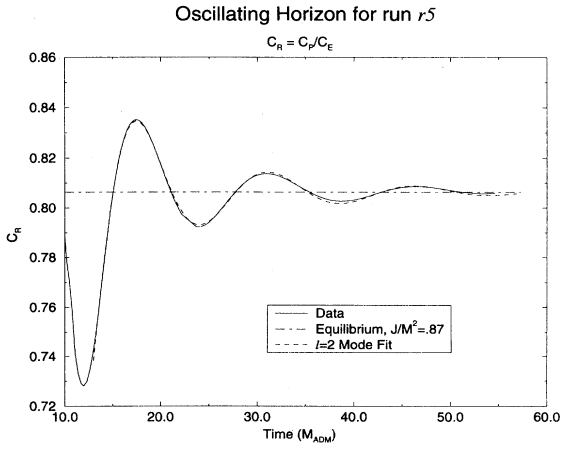

FIG. 2. This figure shows C_r (the ratio of polar to equatorial circumference of the apparent horizon) as a solid line and an $\ell = 2$ quasinormal mode fit form run $r5$. The horizontal short and long dashed line is the offset from sphericity, determined by the fit, showing that the black hole is oscillating about a Kerr hole with rotation parameter $a/m = 0.87$.

$C_r \approx 0.89$ for the run labeled $r4$. In this case the analysis shows the rotation parameter to be $a/m = 0.87$.

Table III gives the results of extracting a/m by this method in column 3 for runs $r0$–$r5$. This table shows that in all cases the value extracted from C_r during the run is very nearly the lower limit $J/M_{\rm ADM}^2$. This means that in the runs under consideration in this paper nearly all the radiation is going into the hole, because the hole achieves nearly the maximum possible mass (or minimum possible rotation parameter).

3. *Embeddings*

A valuable feature of the horizon geometry is its three-space embedding. By embedding the horizon we can obtain a visual impression of its overall distortion in a coordinate-independent way. The Kerr geometry is a sphere in Boyer-Lindquist coordinates, but it is not so when embedded in three-space. Instead it is an oblate spheroid that becomes increasingly flattened along its axis of rotation as its spin increases. If its rotation parameter a/m exceeds $\sqrt{3}/2$, it is impossible to completely embed the figure in flat space, as shown by Smarr [16].

The procedure for finding the embedding starts by defining a new coordinate z which is part of a flat three-metric and is identified with the two-metric of our surface:

$$dz^2 + d\rho^2 + \rho^2 d\phi^2 = B' d\theta^2 + D' d\phi^2. \tag{13a}$$

Solving this expression for z gives

$$z = \int d\theta \sqrt{B' - \left(\partial_\theta \sqrt{D'}\right)^2}, \tag{13b}$$

and

$$\rho = \sqrt{D'}. \tag{13c}$$

This equation is then integrated numerically to obtain the embedding functions $z(\theta)$ and $\rho(\theta)$. In Fig. 3 we show the embedding of the evolving horizon for run $r4$. At time $t = 5M$ the horizon is still frozen and has its initial prolate shape with $C_r = 1.228$. At time $t = 10M$ the horizon has become noticeably oblate, overshooting its equilibrium value, and by the late time of $t = 50M$ it has settled down to very near its equilibrium Kerr value. The dark solid line shows the shape of the Kerr hole with the rotation parameter determined from the procedure above. (The area has been normalized to take account of the difficulty of resolving the peak in A that can cause the area to grow spuriously, as discussed below and in Ref. [9].)

For a Kerr black hole, when the rotation parameter a/m becomes large enough and the integrand of Eq. (13b) becomes imaginary, the embedding ceases to exist. However, this generally happens only over a small portion of the horizon surface, near the symmetry axis. This embedding failure will begin to occur when $a/m = \sqrt{3}/2 \approx 0.87M$. The angle θ (measured from the z axis) at which the embedding should cease to exist can be found. The equation for this angle is

$$\cos^2\theta = \frac{5+3b}{3(b-1)} - \frac{4}{3(1-b)^{2/3}x^{1/3}} + \frac{2x^{1/3}}{3(1-b)^{4/3}}, \tag{14a}$$

where

$$x = 17 + 10b + 3\sqrt{3(11+12b+4b^2)} \tag{14b}$$

and

$$b = \sqrt{1-(a/m)^2}. \tag{14c}$$

Note that for the region $\theta \gtrsim 0.4\pi$ the embedding never disappears.

This effect can actually be used to measure the rotation parameter for rapidly rotating holes. For a dynamic rotating black hole, as shown above the horizon geometry will oscillate about the stationary Kerr shape. For an extremely fast rotator or highly distorted black hole the oscillations may distort the horizon so much that the embedding fails at times during the evolution (or in extreme cases the embedding may never exist). In Fig. 4 we plot the value of θ for which the embedding fails as a function

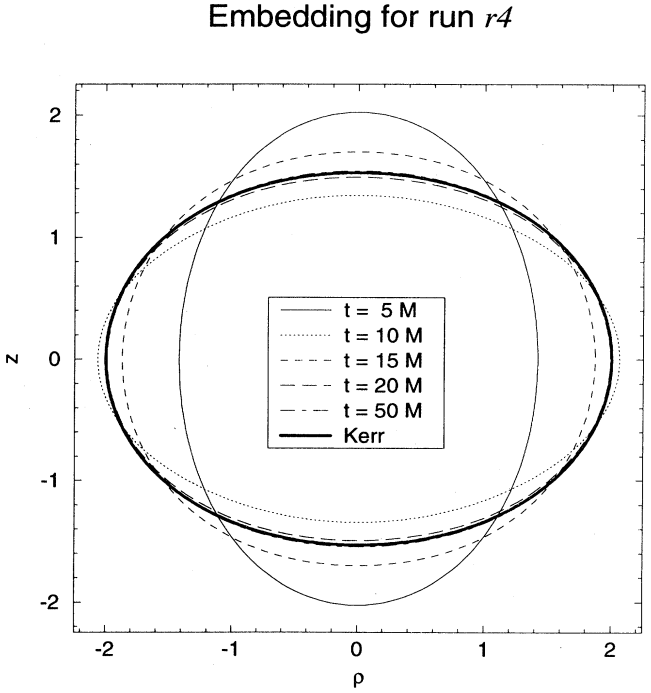

FIG. 3. This figure shows the three-space embedding of the distorted rotating black hole run labeled $r4$ at various times. Although the black hole's apparent horizon is initially prolate, it eventually settles down to the appropriate oblate Kerr black hole shape denoted by a dark solid line.

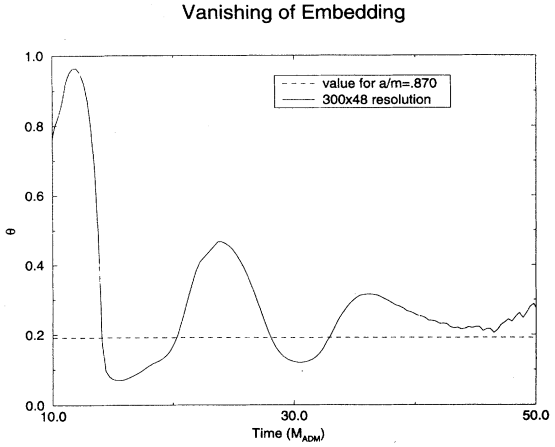

FIG. 4. This plot shows the position at which the Euclidean three-space embedding of the apparent horizon vanishes for run labeled $r5$, a Bowen-York rotating black hole, with angular momentum parameter $J = 15$ (solid line). As discussed in the text, for rapidly rotating holes the horizon embedding fails near the axis at an angle determined by the rotation parameter. The dashed line shows the angle at which the embedding fails for an "equilibrium" Kerr black hole with $a/m = 0.87$.

of time for the case $r5$. This is a pure Bowen-York hole with $J = 15$, corresponding to $a/m = 0.87$.

The run labeled $r5$ is the fastest rotating black hole we have simulated to date, and it pushes the limits of our code, but it nevertheless produces a good result, in agreement with theory. The straight horizontal line represents the embedding limit of the analytic Kerr solution with the given value of $a/m = 0.87$, which was the rotation parameter that was extracted from the oscillation about C_r as discussed above. Note that this black hole horizon is *never* globally embedded in three-dimensional Euclidean space, although the horizon always exists. Note also that by measuring the horizon geometry, we can determine the rotation parameter at least two different ways: by measuring C_r as in Fig. 1 (see discussion above) and by measuring the angle at which the embedding ceases to exist (although this only works for holes which have $a/m > \sqrt{3}/2$). Furthermore, these measurements agree with estimates of the rotation parameter determined from the initial data alone.

B. Horizon history diagrams

As we have shown in Ref. [9] it is useful to construct a "horizon history" embedding diagram that shows the evolution of the surface in time. In order to bring out details of the local curvature of this surface, we also compute the Gaussian curvature κ of the horizon surface and map it to a colormap or greyscale. For details of this construction we refer the reader to Ref. [9], but for reference we present the formula for Kerr here:

$$\kappa = \frac{8\,[-1 + 5\,b - 3\,\cos(2\,\theta) + 3\,b\,\cos(2\,\theta)]}{(1+b)\,m^2\,[3 + b + \cos(2\,\theta) - b\,\cos(2\,\theta)]^3}, \quad (15)$$

where $b = \sqrt{1 - a^2/m^2}$ as before. The mapping of the Gaussian curvature onto the surface helps to bring out small deviations in the local curvature of the surface that would not be apparent in the embedding diagram itself.

In Fig. 5 we show a horizon history embedding diagram for the case $o1$, which is an odd-parity distorted nonrotating black hole. As we discuss in detail in Sec. V, this data set has predominantly $\ell = 3$ radiation (99% of the total energy radiated is carried in this mode). As in the cases shown in Ref. [9], each ℓ-mode pattern is qualitatively different from the ones studied previously. In Fig. 6 we show a similar diagram for the run labeled $o2$, which has a significant $\ell = 5$ component. Again, the pattern is qualitatively different from the $\ell = 3$ (or $\ell = 2$ or $\ell = 4$) pattern, and has not been seen before.

These distinctive patterns can be understood by analyzing the expression for the Gaussian curvature. The metric variable F enters the Gaussian curvature as a second-order term (to first order it vanishes identically). This function carries the odd-parity radiation in our gauge, as discussed below. Therefore, if F oscillates predominantly at the $\ell = 3$ normal mode frequency denoted by $\omega_{\ell=3}$, then the period of oscillation one will see in the Gaussian curvature plot will not be $\omega_{\ell=3}$ as a result of this nonlinearity. Instead one will see $2\omega_{\ell=3}$, and so the pattern cycle will repeat twice as quickly as it would have if F had entered the Gaussian curvature to linear order.

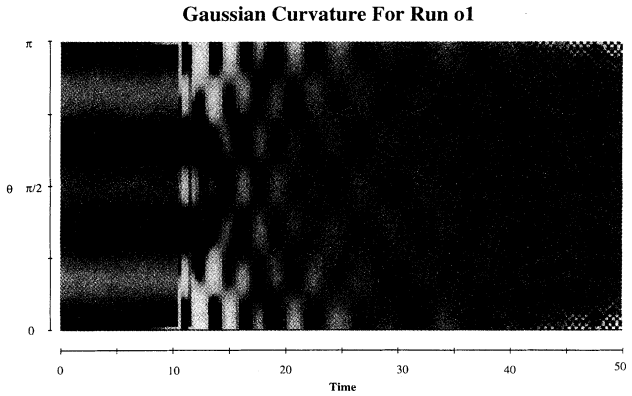

FIG. 5. We show the horizon history diagram for the run labeled $o1$. The Gaussian curvature κ is mapped to a gray scale on the surface of the horizon. The vertical axis gives the angular location on the horizon, and the horizontal axis traces out the time development. As discussed in the text, we see a pattern that repeats at twice the $\ell = 3$ QNM frequency in accordance with theoretical expectations. In the figure, dark regions are more highly curved than light regions.

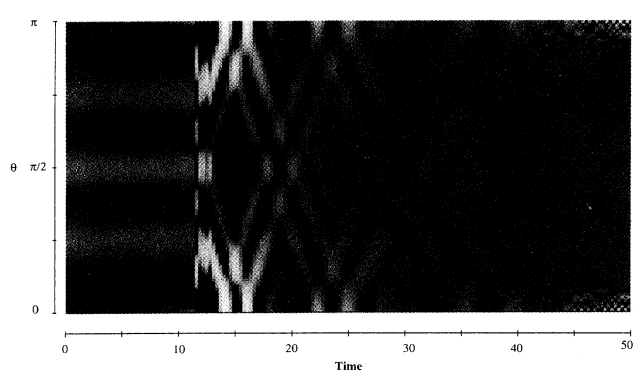

FIG. 6. In this plot we show the horizon history diagram for the run labeled *o2*. Hence the Gaussian curvature shows a diamond pattern, a result of the mixing of several frequencies of the $\ell = 3$ and $\ell = 5$ quasinormal modes. In the figure, dark regions are more highly curved than light regions. See text for details.

This is what one sees in Fig. 5. The pattern repeats every $t \approx 5.24M$ instead of every $t \approx 10.48M$, which is the period of the $\ell = 3$ fundamental mode.

In Fig. 6 the $\ell = 5$ modes are present to a much stronger degree, and so we see a mixture of the $\ell = 3$ and $\ell = 5$ modes. This creates a diamond pattern reminiscent of the diamond pattern seen on the surfaces of even-parity black hole horizons generated with an $n = 4$ perturbation, as described in Ref [4]. In general, however, this pattern is more complicated than the $n = 4$ pattern, as it should include four frequences: $2\omega_{\ell=3}$, $\omega_{\ell=3} \pm \omega_{\ell=5}$, and $2\omega_{\ell=5}$.

IV. FAR ZONE PHYSICS

A. Wave mode extraction

In previous sections we have analyzed properties of the near zone features of these new black hole data sets, focusing on geometric measures of the horizon. These effects provide important probes of the physics of the near zone, and can also be used to determine important properties of evolving black holes that may not be known, but for the most part these effects are not measurable by gravitational wave experiments such as the Laser Interferometric Gravitational Wave Observatory (LIGO). In this section we turn to analysis of the physics of the far zone, where important features such as gravitational waves can actually be observed.

One of the principal features of a dynamical black hole spacetime which has been possible to study analytically is linearized gravitational waves. Therefore, it is useful for us to measure them in highly distorted black hole spacetimes to determine information that linear theory cannot predict, such as the final mass of a black hole in a perturbed spacetime or the waveform emitted during the nonlinear generation of gravitational waves, and to provide several useful checks of our code. Although the processes that generate these waves may be highly nonlinear, far from the hole the waves may be treated as linear perturbations on a fixed background. For all the simulations presented in this paper we extracted the radiation at a distance $r = 15M$.

The radiation energy in a black hole spacetime is described by certain gauge-independent variables constructed from the metric and its derivatives. The technique was originally developed by Abrahams and Evans [18] and applied to black hole spacetimes in Ref. [3]. There are two classes of gauge-invariant radiation quantities representing the two degrees of freedom of the field, even parity and odd parity. Both are present in our spacetimes and we describe them below.

1. *Even parity*

We used the same wave extraction routines for the even-parity wave forms as used in Ref. [3]. The routines were developed to extract waveforms from perturbed *Schwarzschild* black hole spacetimes that oscillate about a spherical background. Because the distorted *Kerr* metric does not settle down to something that is spherical, but rather it settles down to something oblate, we should expect to see this effect in the extraction process, resulting in an offset in the $\ell = 2$ and $\ell = 4$ waveforms. Thus, the wave does not oscillate about zero, but instead will be offset from zero depending on both the rotation parameter and the radius at which the wave is extracted.

However, the level of this offset is small and its variation rather too sensitive so that we have not been able to use it to measure the rotation parameter reliably. As shown below, we do see this effect in waveforms extracted from distorted rotating black holes, and the offset value is related to the rotation parameter as expected. The offset we obtain from the waveforms is of the right general magnitude and sign for a given rotation parameter. In principal one can account for the fact that the system is a perturbed Kerr black hole, but to date we have not carried out this analysis. However, as we show below, the extraction assuming a spherical Schwarzschild background can be quite useful without modification.

The even-parity wave extraction is given here. Note that this extraction formula assumes a Schwarzschild background. For each ℓ mode we can extract independent radiation waveforms. The gauge-invariant, even-parity wave function is given by

$$\psi^{\rm even} = \sqrt{\frac{2(\ell-1)(\ell+2)}{\ell(\ell+1)}}\,\frac{\left(4rS^2k_2 + \ell(\ell+1)rk_1\right)}{\Lambda} \qquad (16a)$$

and

$$\Lambda = \ell(\ell+1) - 2 + \frac{6M}{r}, \qquad (16b)$$

where the Moncrief functions [19] are given by

$$k_1 = K + Sr\frac{\partial G}{\partial r}, \qquad (16c)$$

$$k_2 = \frac{H_2}{2S} - \frac{1}{2S^{\frac{1}{2}}}\frac{\partial}{\partial r}\left(rS^{-\frac{1}{2}}K\right), \tag{16d}$$

with

$$S = 1 - \frac{2M}{r}, \tag{16e}$$

$$r = e^{\eta}, \tag{16f}$$

and finally the Regge-Wheeler [20] perturbation functions are defined in terms of the three-metric via

$$H_2 = \frac{2\pi}{\hat{A}^2}\int_0^{\pi} \Psi^4 A\, Y_{\ell 0} \sin\theta d\theta, \tag{16g}$$

$$\hat{A}^2 = \frac{1}{2}\int_0^{\pi} \Psi^4 A \sin\theta\, d\theta, \tag{16h}$$

$$G = \frac{2\pi}{R^2}\int_0^{\pi} \Psi^4 \frac{(B-D)\left(-\cos\theta\, Y_{l0,\theta} + \sin\theta\, Y_{l0,\theta,}\right) d\theta}{\ell\,(\ell+1)\,(\ell+2)\,(\ell-1)}, \tag{16i}$$

$$K = \frac{\ell\,(\ell+1)}{2}G + \frac{\pi}{R^2}\int_0^{\pi} \Psi^4\,(B+D)\sin\theta\, Y_{\ell 0} d\theta, \tag{16j}$$

$$R^2 = \frac{1}{2}\int_0^{\pi} \Psi^4\, B\, \sin\theta\, d\theta. \tag{16k}$$

With the normalization of ψ given above one can show that the total radiated energy in each ℓ mode is given by

$$E = \frac{1}{32\pi}\int dt\,(\partial_t \psi)^2\,. \tag{17}$$

Complete details of this extraction procedure are provided in Ref. [3].

2. Odd parity

In terms of the Regge-Wheeler formalism [20] there are various ways to construct the odd-parity gauge-invariant variable that measures the radiation in the system [19]. These measures are not linearly independent, and each is constructed from two of the variables E, F, and β^{ϕ}, which correspond to the Regge-Wheeler variables h_1, h_2, and h_0 after appropriate angular integrals have been performed. The gauge-dependent Regge-Wheeler variables can be extracted from the metric as

$$h_0 = \sqrt{\frac{(\ell+1)!}{(\ell-1)!}}\oint d\Omega\, \beta_{\phi}\, \partial_{\theta} Y_{\ell 0}, \tag{18a}$$

$$h_1 = \sqrt{\frac{(\ell+1)!}{(\ell-1)!}}\oint d\Omega\, \Psi^4 E\, \partial_{\theta} Y_{\ell 0}, \tag{18b}$$

and

$$h_2 = \frac{1}{2}\sqrt{\frac{(\ell+2)!}{(\ell-2)!}}\oint d\Omega\, \Psi^4 F\,(\partial_{\theta} - \cot\theta)\,\partial_{\theta} Y_{\ell 0}. \tag{18c}$$

From these perturbation functions one can construct the following gauge-invariant quantities, two of which are given in Ref [21]:

$$\psi_{02} = h_0 + \frac{1}{2}\partial_t h_2, \tag{19a}$$

$$\psi_{01} = r^2\partial_r\left(\frac{h_0}{r^2}\right) - \partial_t h_1, \tag{19b}$$

and

$$\psi_{12} = h_1 + \frac{1}{2}r^2\partial_r\left(\frac{h_2}{r^2}\right). \tag{19c}$$

In our code we have used our gauge freedom to eliminate the metric function E (h_1) and the method we use to extract the radiation is effectively Eq. (19c). It is also possible to measure the odd-parity radiation through Eq. (19a) as we show below. Note that for the odd-parity case, there is no "nonspherical odd-parity" part in a Kerr black hole (in ψ_{12}) and so there is no offset expected or observed for these waveforms.

The particular energy integrals for the odd-parity modes are given here. Note that these expressions are specific to our gauge and a flat space background metric. We first normalize our gauge-invariant odd-parity wave function, based on Eq. (19c), as

$$\psi^{\rm odd}_{\ell=3} = \int_0^{\pi} d\theta\, \frac{1}{2}\sqrt{105\pi}\cos\theta\sin^3\theta\partial_{\eta} F \tag{20a}$$

and

$$\psi^{\rm odd}_{\ell=5} = \int_0^{\pi} d\theta \frac{1}{16}\sqrt{1155\pi}\,[5\cos\theta + 3\cos(3\theta)]\sin^3\theta\partial_{\eta} F. \tag{20b}$$

For general ℓ the energy expression is this

$$\psi^{\rm odd} = \int_0^{\pi} 2\pi\sqrt{2\frac{(\ell-2)!}{(\ell+2)!}}d\theta\,\partial_{\eta} F\sin\theta\,(\partial_{\theta} - \cot\theta)\,\partial_{\theta} Y_{\ell 0}. \tag{21}$$

In principle one can extract arbitrarily high ℓ modes. In practice we have only examined the $\ell = 3$ and $\ell = 5$ modes to date. With these normalizations, the energy radiated by each ℓ mode is given by

$$E = \frac{1}{32\pi}\int dt\psi^2, \tag{22}$$

as in Ref. [21].

B. Measurement of frequencies

To analyze quantitatively the frequency spectrum of our radiation we used the following Fourier technique. Because the quasinormal modes of black holes are all damped, the Fourier spectrum of their frequencies will be spread out. To counter this effect, before analyzing a waveform we premultiply it by a factor $\exp(\lambda t)$, where λ is chosen to approximately cancel the effects of the damping (see Ref. [22] for a discussion of such techniques). As

it happens, the damping time for the fundamental mode is given approximately by $\lambda \approx 0.09/M$, relatively independent of the ℓ value, and so this technique is helpful for all modes.

We next decompose the frequency spectrum using the procedure described below. The technique used here to analyze the waveforms is preferable to a fast Fourier transform (FFT), since an FFT may provide poor frequency resolution for the wavelengths under study unless the sampling interval (ΔT) is quite long. For example, to distinguish between the peaks in $\ell = 2$ and $\ell = 3$ QNM's would require a "sampling period" greater than $\Delta T \approx 60M$ of oscillations. The Fourier technique we present below, combined with the premultiplication technique, can distinguish between them with only about $\Delta T \approx 17M$ of oscillations. We approximate the Fourier transform function and its inverse by

$$\hat{f}(\omega) = \frac{1}{\sqrt{2\pi}} \int_{-\infty}^{\infty} f(t) e^{-i\omega t} dt \approx \sum_i f_i \hat{\delta}_i(\omega) \Delta t, \quad (23a)$$

$$f(t) = \frac{1}{\sqrt{2\pi}} \int_{-\infty}^{\infty} \hat{f}(\omega) e^{i\omega t} d\omega \approx \sum_i f_i \delta(t - t_i) \Delta t, \quad (23b)$$

where we have defined

$$\delta(t - t_i) = \frac{1}{\sigma\sqrt{\pi}} e^{-(t-t_i)^2/\sigma^2} \quad (23c)$$

and

$$\hat{\delta}_i(\omega) = e^{-i\omega t_i - \sigma^2\omega^2/4}. \quad (23d)$$

In the above equations, $f(t)$ is the Regge-Wheeler or Zerilli function, (f_i, t_i) are the set of points produced by the numerical code [we should find that $f_i \approx f(t_i)$], and t is the time. The value of σ was set to Δt.

Note that the presence of the first overtone of a quasinormal mode frequency cannot be as easily detected with this technique (since the damping is so much greater). It manifests as a small shift in the position of the peak of the fundamental mode. The position of the peak will also be affected by the artificial growth in the mass that occurs at late times, which is manifested in the waveform by lengthening of the wavelength of the radiation as discussed in Ref. [3]. This artificial lengthening will effectively add a mixture of other frequencies to the spectrum, further broadening the peak.

V. RESULTS AND DISCUSSION

In this section we discuss results from evolutions of the initial data sets listed in Tables I and II, combining many of the analysis techniques discussed in the previous sections. Together these tools provide a thorough and remarkably consistent physical picture of the evolution of these black hole spacetimes.

A. Odd-parity distorted Schwarzschild black holes

In this section we give results for evolution of the new class of data sets we constructed and discussed briefly in Ref. [5]. These evolutions correspond to runs labeled $o1$ and $o2$. These data sets do not possess angular momentum, but they do possess odd-parity radiation, in contrast to the "Brill wave plus black hole spacetimes" discussed previously in Ref. [1]. Strictly speaking, they are odd-parity distorted Schwarzschild black holes, and not rotating holes. Nevertheless, the odd-parity distortions give rise to "rotationlike" features. We note that these black hole data sets also contain even-parity radiation, although of a much lower amplitude.

The run labeled $o1$ represents a spacetime with virtually only an $\ell = 3$ distortion, as almost all the energy is radiated in that mode. Figure 7 shows the $\ell = 3$ waveform extracted by the gauge-invariant waveform extraction method described in Sec. IV A 2 above. As one can see, it is almost impossible to distinguish the fit from the data. As we show in Table III, 99.96% of the total energy radiated is carried by the $\ell = 3$ mode. In Fig. 8 we show the $\ell = 5$ waveform extraction for the same run. It is interesting to note that even though it does not contribute significantly to the energy, and the signal amplitude is nearly four orders of magnitude smaller than the $\ell = 3$ signal, the $\ell = 5$ signal is still easily fit to the proper mode.

For run $o1$ we extracted the $\ell = 3$ radiation mode from both β^ϕ and F. Both extractions are plotted in Fig. 9. The solid line illustrates the extraction from the shift; the dotted line traces the value extracted from F. The waveform extracted from β^ϕ was normalized so that it had the same lower bound as the waveform extracted from F. This shows that it is possible to perform the extraction from the shift, although we have only done so for this test.

Next we consider the run labeled $o2$, which has a larger $\ell = 5$ signal. The $\ell = 5$ extracted mode, shown in Fig. 10, matches the fit to the quasinormal modes quite well, as in

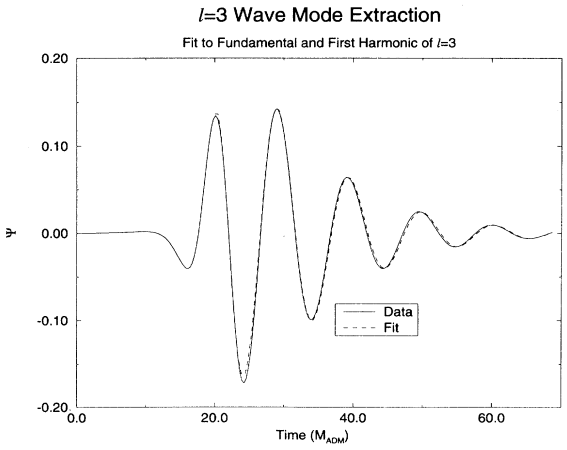

FIG. 7. We plot the extraction of the $\ell = 3$ waveform from the odd-parity distorted nonrotating hole, run labeled $o1$. The dashed line shows the fit of this waveform to the two lowest $\ell = 3$ quasinormal modes. Practically all of the radiated energy is in this mode.

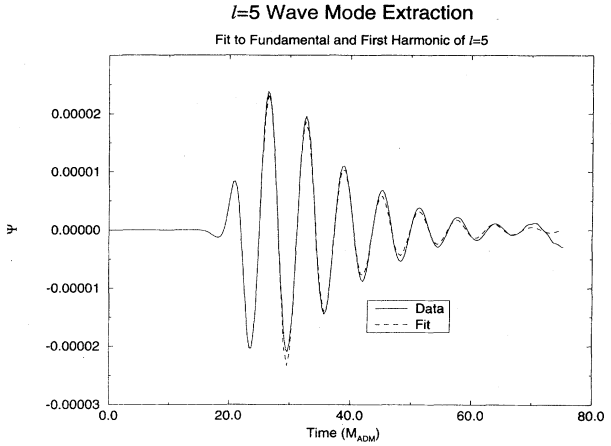

FIG. 8. This figure shows the numerically extracted $\ell = 5$ waveform and its fit to the two lowest $\ell = 5$ quasinormal modes for the run labeled $o1$.

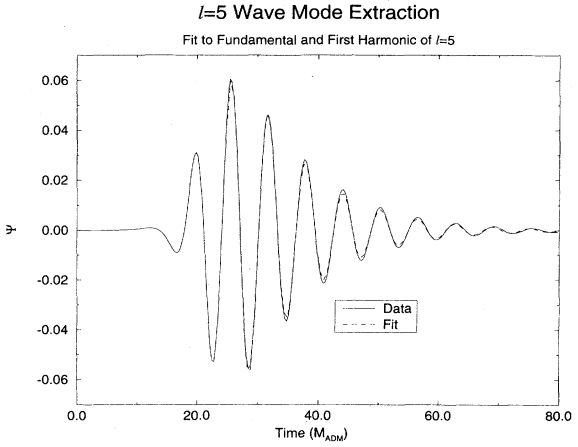

FIG. 10. We show the extraction of the $\ell = 5$ waveform from an odd-parity distorted nonrotating hole, run labeled $o2$. It is clear that the fit (dashed line) agrees well with the numerically extracted function (solid line).

the previous case. (The $\ell = 3$ waveform, not shown here, matches its quasinormal mode fit with the same level of accuracy as in the previous case $o1$.) After measuring the $\ell = 5$ frequency from our extracted waveform via the Fourier transform technique discussed in Sec. IV B above, we discovered that its quasinormal modes were not tabulated in the literature. We computed the real part of the frequency to be 1.00 ± 0.01. Subsequent calculations by Edward Leaver, based on black hole perturbation theory [23], yield the result 1.012 which agrees with our result to within 1%. In Fig. 11 we compare the analytic $\ell = 5$ frequency with the Fourier transform (as implemented by the technique described above) of our data for the run labeled $o2$. A dotted line is placed on the graph to show where the peak should be for a pure $\ell = 5$ wave. The secondary peaks do not represent real frequencies; rather, they are an artifact of the extraction process.

Finally, we turn to a calculation of the energies and masses in the system. The mass of the apparent horizon for the run labeled $o1$ is plotted in Fig. 12. The solid line shows the instantaneous mass of the horizon, defined by Eq. (10), and the long dashed line represents the to-

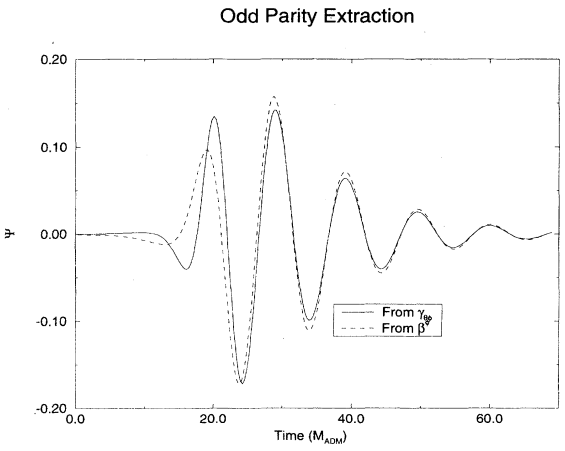

FIG. 9. In this figure we compare the $\ell = 3$ waveform extracted from the ϕ shift β^ϕ (dashed line) and from the metric variable $F = g_{\theta\phi}/\Psi^4$ (solid line), where Ψ is the conformal factor. Although we generally use the extraction based on the three-metric, this demonstrates that other techniques can be used. Note that the waveform extracted from the β^ϕ was normalized to have the same lower bound as the shift extracted from F.

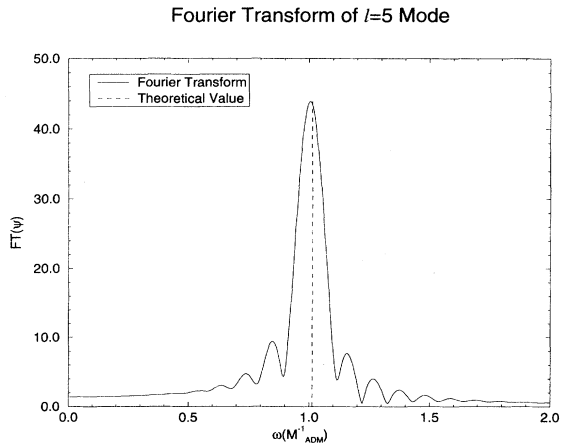

FIG. 11. This figure shows a Fourier transform of the data extracted from the run labeled $o2$. The dotted line shows real part of the $\ell = 5$ frequency, computed via black hole perturbation theory.

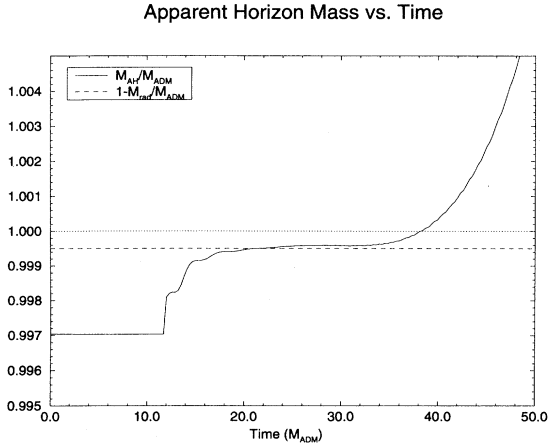

FIG. 12. This figure shows the apparent horizon mass defined in the text, for the run labeled $o1$ normalized by the ADM mass (solid line). After about $t = 40M$ the area of the horizon slowly drifts up as a result of difficulties in resolving metric functions, causing an overestimation of the horizon mass. (See text.) The short-dashed line is drawn at 1, representing the total mass of the spacetime. The gap between the short-dashed and long-dashed lines is the amount of energy emitted through radiation. As one can see, the mass of the horizon and the energy of the radiation add up to the ADM mass.

tal energy radiated away from the black hole during the evolution. All energies in this plot are normalized to the ADM mass, and therefore it can readily be seen that the sum of the final apparent horizon mass (as measured at $t = 25M$) and the energy emitted through radiation (as calculated by integrating the even- and odd-parity radiation functions for $\ell = 2, 3, 4$, and 5 for the entire time of the run) add up to the ADM mass. The very slight dip in the mass at around $30M$ becomes less noticeable with increasing resolution.

After about $t = 35M$ the peak developing in the radial metric function is not adequately resolved. As the horizon is located near this peak, as discussed in paper I, its area is not accurately computed after this time. However, the simulation can be continued until about $t = 100M$ and accurate waveforms can be extracted throughout. Furthermore, the calculations of the *shape* of the horizon continue to be accurate throughout the evolution, even though the area becomes inaccurate.

B. Kerr black holes

Although a Kerr black hole is stationary and not dynamical, it does provide a useful test case for evolution. Furthermore, as it is the "equilibrium" black hole about which all other black hole spacetimes considered in the paper oscillate, it is useful to study its properties.

Because there is no radiation in the system, we do not expect the horizon to oscillate. In paper I we used the Kerr black hole as a test case to show that our code was able to evolve the Kerr spacetime accurately by computing its angular momentum during the evolution. Here we apply two of the near zone measurements developed in Sec. III for these spacetimes to show the numerical properties of these evolved black holes.

In Fig. 13 we show the mass $M_{\rm AH}$ of an $a/m = 0.48$ black hole (labeled $k1$) as a function of time for three different resolutions. The horizon mass should be strictly conserved and equal to the ADM mass for a stationary black hole. The high resolution (300×30) mass is plotted as a solid line, the medium resolution (150×24) mass is plotted as a dotted line, and the low resolution (75×12) mass is plotted as a dashed line. The mass is nearly constant until the large peaks discussed in paper I develop and cannot be adequately resolved. By $t = 40M$, the error in the mass is still less than 0.1% at all but the lowest resolution and by $t = 60M$ the error is still only 0.5%. Although the apparent horizon mass does not exactly equal the ADM mass, it is within the error expected given the level of angular resolution of the horizon. The jaggedness of the lower resolution lines is a numerical effect. A new bump occurs each time the interpolator in the horizon finder changes the set of grid zones it uses. It is only visible because of the small range of $M_{\rm AH}/M_{\rm ADM}$ which we are viewing.

In Fig. 14 we show a similar graph for run $k2$, corresponding to a Kerr black hole with rotation parameter $a/m = 0.68$. Despite the higher rotation, all features noted for run $k1$ are preserved to a high degree. Because there is more angular variation in the metric, there is slightly less agreement between $M_{\rm AH}$ and $M_{\rm ADM}$.

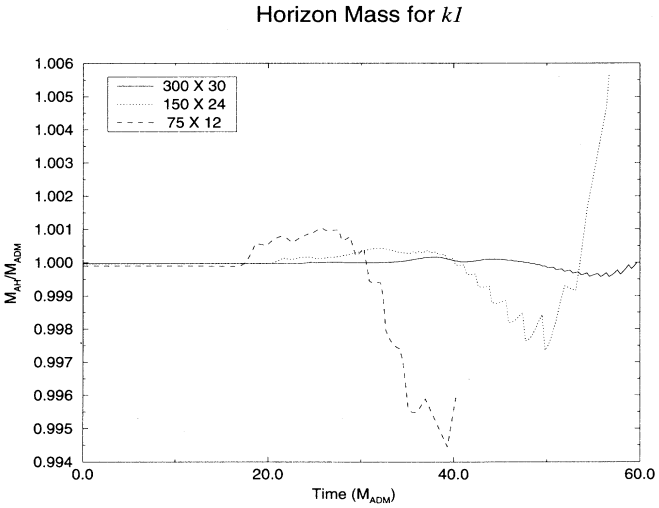

FIG. 13. This figure shows the apparent horizon mass for run $k1$ ($a/m = 0.48$) at three resolutions. It is clear that the apparent horizon mass becomes more constant and agrees better with the ADM mass as the resolution is increased. At all but the lowest resolution we have about 0.5% accuracy in the apparent horizon mass at the late times shown.

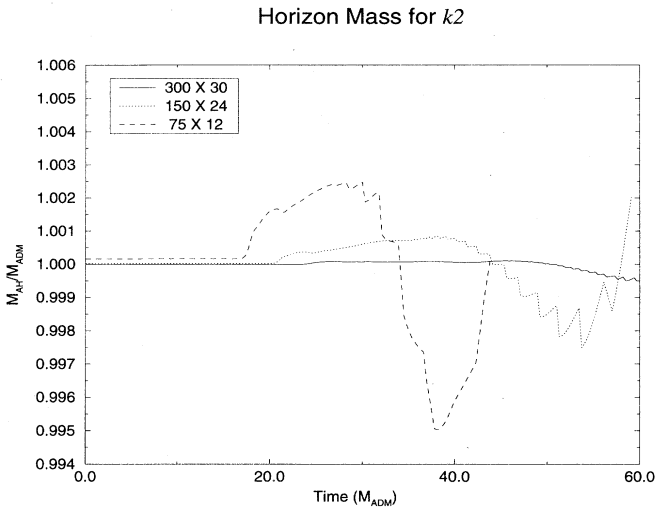

FIG. 14. This figure shows the apparent horizon mass for run $k2$ ($a/m = 0.68$) at three resolutions. It is clear that the apparent horizon mass becomes more constant and agrees better with the ADM mass as resolution is increased. At all but the lowest resolution we have about 0.1% accuracy in the apparent horizon mass.

C. Distorted Bowen-York black hole

In this section we discuss results for the six initial data sets labeled $r0$–$r5$. This represents a sequence of distorted black holes with increasing values of the rotation parameter, a/m, beginning with a nonrotating case, labeled $r0$.

The first case we discuss is run $r0$, which has the same construction as the "Brill wave plus black hole spacetime" discussed in detail in Ref. [1]. This spacetime was evolved with an antisymmetric lapse across the black hole throat, and so, although the data set is in the same class as those evolved in Ref. [24], it has been evolved with a new code capable of handling rotating black holes and with a different slicing condition. The same simulation was discussed in paper I, where a comparison of metric functions was made to the evolution obtained with the code described in Ref. [1]. In Fig. 15 and Fig. 16 we show the now familiar $\ell = 2$ and $\ell = 4$ waveforms extracted from the evolution, with a fit of the two lowest quasinormal modes in each case. The match is excellent. It is also important to note that no odd-parity radiation is present in this system and there are no $\ell = 3$ or $\ell = 5$ waveforms to show. (It is important to point out that odd parity does *not* mean odd ℓ, and even parity does *not* mean even ℓ. It simply happens that with equatorial plane symmetry, which is present here, there are no odd-ℓ, even-parity modes or even-ℓ, odd-parity modes.) The new dynamical variables used in this evolution remain exactly at zero when there is neither odd-parity distortion nor rotation.

In Fig. 17 we show the mass of the apparent horizon for run $r0$, as defined in Sec. III A above. Note that initially it does not change, as the antisymmetric lapse freezes the evolution at the throat where the apparent horizon is found on the initial data set. Then at about time $t = 10M$, the horizon is found out at a larger radius and evolves slowly outward, its mass increases as more gravitational wave energy crosses the horizon surface into the hole. (This "jumping out" of the horizon is a common property of all simulations we have performed with an antisymmetric slicing condition as discussed in Sec. III A above.) After a time of about $t = 25M$, there is a slow upward drift in the mass as a result of difficulties in resolving the peak in the radial metric function A that develops near the horizon [9]. By this time, nearly all of the ingoing gravitational wave energy has entered the black hole, and we compute the final mass of the hole to be $M_{\rm AH} = 0.915 M_{\rm ADM}$. We also have computed the

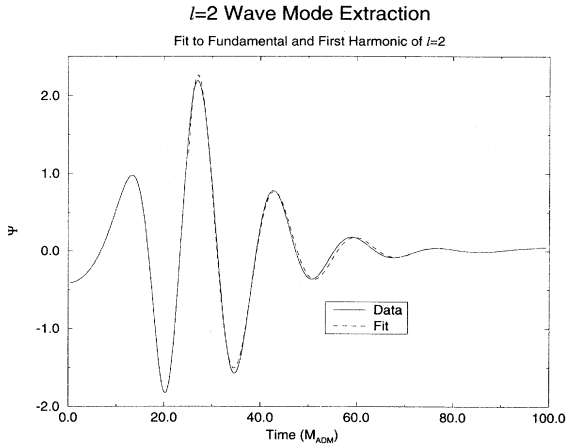

FIG. 15. This figure shows the numerically extracted $\ell = 2$ waveform (solid line) and the least squares fit to the two lowest $\ell = 2$ quasinormal mode for this distorted nonrotating black hole. This run was labeled $r0$.

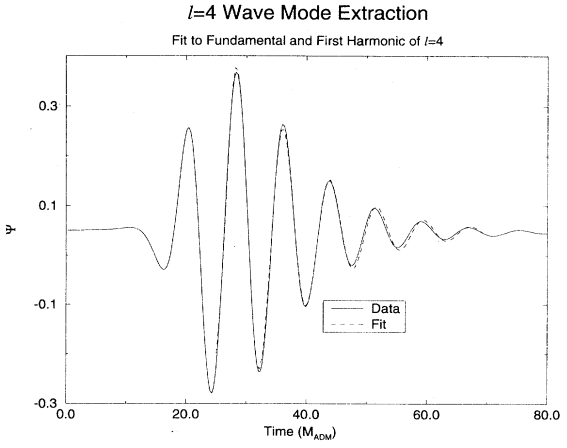

FIG. 16. This figure shows the numerically extracted $\ell = 4$ waveform and its fit to the two lowest $\ell = 4$ quasinormal modes for the run labeled $r0$.

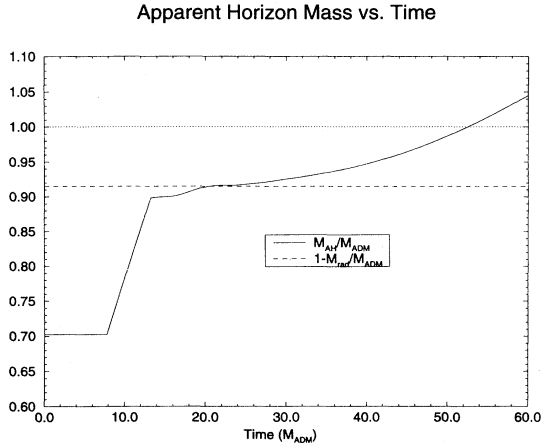

FIG. 17. This figure shows the apparent horizon mass defined in the text, for the run labeled $r0$ normalized by the ADM mass (solid line). The short-dashed line is drawn at 1, representing the total mass of the spacetime. The gap between the short-dashed and long-dashed lines is the quantity of radiation emitted. The mass of the horizon and the energy of the radiation add up to the ADM mass.

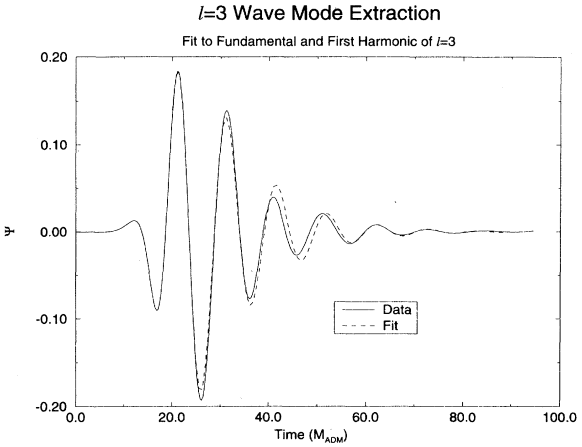

FIG. 18. This figure shows the numerically extracted $\ell = 3$ waveform and its fit to the two lowest $\ell = 3$ quasinormal modes for the run labeled $r1$.

total energy radiated through the dominant $\ell = 2$ mode, as shown in Table IV, and plot it in Fig. 17. Note that all the energy is accounted for to a high degree of accuracy. The total energy radiated by the black hole, as computed by integrating the Zerilli function, plus the final mass of the black hole, as determined by the mass of the apparent horizon, gives the total ADM mass of the spacetime, as one would expect.

Next we turn to the run labeled $r1$. This calculation is similar to the previous run except that a noticeable amount of energy is now being radiated in the $\ell = 3$ quasinormal mode, as shown in Fig. 18. The value of a/m is extracted from C_r, demonstrating that this technique is effective for small values of a/m, as shown in Fig. 19 (although $a/m = 0.35$ is considered to be "small" in this study, the vast majority of black holes in the real universe are probably smaller than this [25]).

Both runs $r2$ and $r3$ were typical of many simulations. Each provides waveforms that fit equally as well as $r4$, each locks on to the appropriate limit slice, and in both cases the radiation energy plus the final apparent horizon mass add up to the ADM mass. We show the plots for the radiation in the $\ell = 2$, 3, 4, and 5 modes for run $r2$ in Figs. 20, 21, 22, and 23, respectively. In each case we fit the wave function to the fundamental and first harmonic mode for the appropriate value of ℓ. The value of a/m used in the frequency fits was derived from the value extracted from the apparent horizon, although it made very little difference whether the dependence of the QNM frequencies on the rotation parameter was accounted for. Except in the case of extreme rotations, the QNM frequencies depended only weakly on a/m [23,26]. In the

TABLE IV. This table shows the total energy emitted as radiation divided by the ADM mass in the rightmost column, and it shows the fraction of this energy emitted in the first four quasinormal modes of the black hole spacetime.

Case	$M_{\rm rad}^{\ell=2}$	$M_{\rm rad}^{\ell=3}$	$M_{\rm rad}^{\ell=4}$	$M_{\rm rad}^{\ell=5}$	$M_{\rm rad}^{\rm total}/M_{\rm ADM}$
$r0$	94.0%	0.0%	6.0%	0.0%	8.37×10^{-2}
$r1$	94.9%	2.0%	2.8%	0.3%	3.40×10^{-2}
$r2$	94.8%	3.4%	1.5%	0.3%	1.84×10^{-2}
$r3$	93.9%	5.2%	0.7%	0.2%	9.41×10^{-3}
$r4$	92.1%	7.0%	0.6%	0.2%	8.30×10^{-3}
$r5$	95.7%	4.1%	0.2%	0.02%	1.00×10^{-3}
$o1$	0.05%	99.9%	0.02%	0.0001%	1.06×10^{-4}
$o2$	0.06%	78.9%	0.00%	21.0%	2.88×10^{-4}
$k1$	NA	NA	NA	NA	5.66×10^{-8}
$k2$	NA	NA	NA	NA	2.85×10^{-7}

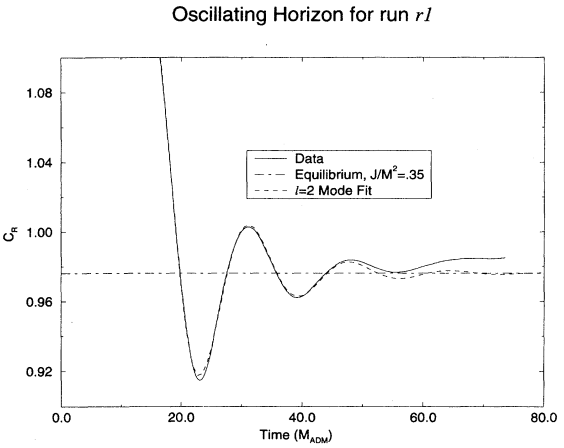

FIG. 19. This figure shows C_r (the ratio of polar to equatorial circumference of the apparent horizon) as a solid line and an $\ell = 2$ quasinormal mode fit from run $r1$. The long and short dashed line is the offset from sphericity, determined by the fit, showing that the black hole is oscillating about a Kerr hole with rotation parameter $a/m = 0.35$.

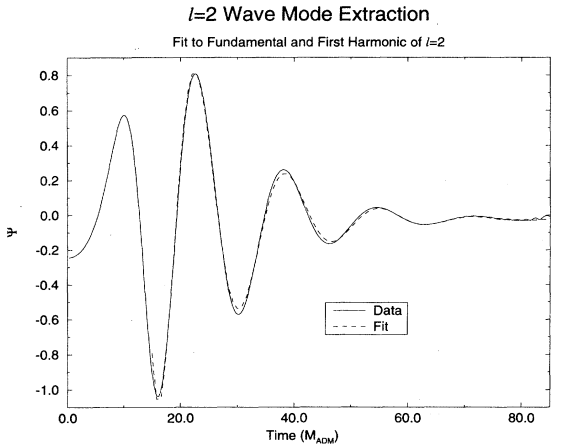

FIG. 20. This figure shows the numerically extracted $\ell = 2$ waveform and its fit to the two lowest $\ell = 2$ quasinormal modes for the run labeled $r2$.

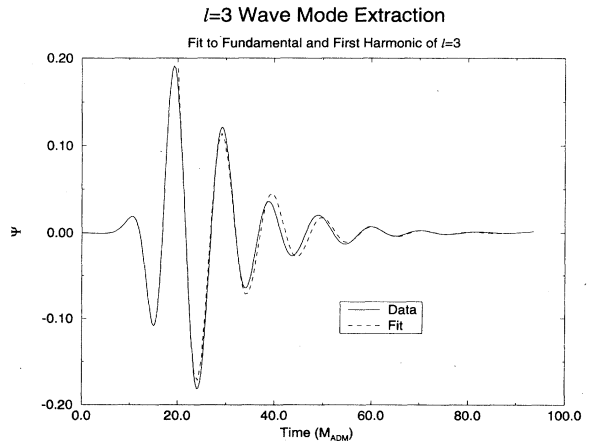

FIG. 21. This figure shows the numerically extracted $\ell = 3$ waveform and its fit to the two lowest $\ell = 3$ quasinormal modes for the run labeled $r2$.

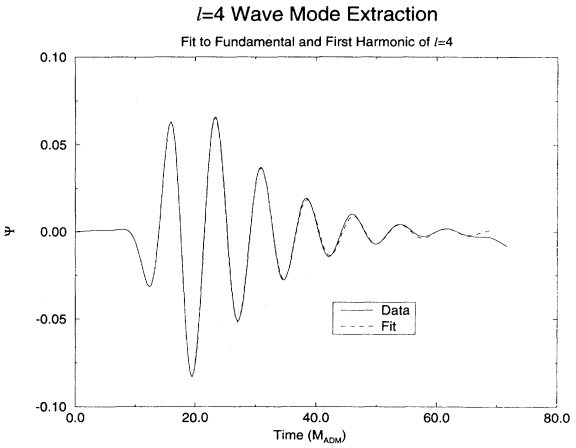

FIG. 22. This figure shows the numerically extracted $\ell = 4$ waveform and its fit to the two lowest $\ell = 4$ quasinormal modes for the run labeled $r2$.

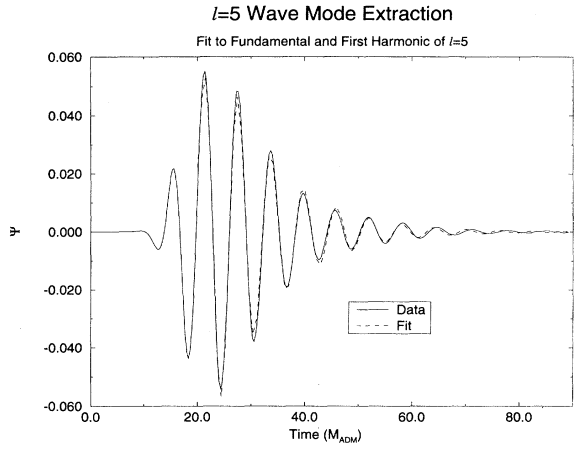

FIG. 23. This figure shows the numerically extracted $\ell = 5$ waveform and its fit to the two lowest $\ell = 5$ quasinormal modes for the run labeled $r2$.

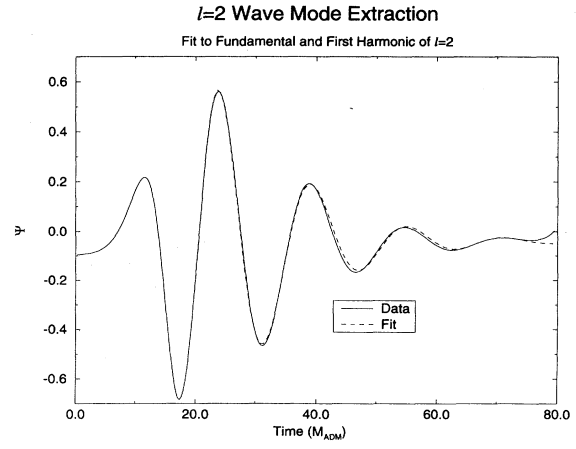

FIG. 24. This figure shows the numerically extracted $\ell = 2$ waveform and its fit to the two lowest $\ell = 2$ quasinormal modes for the run labeled $r4$.

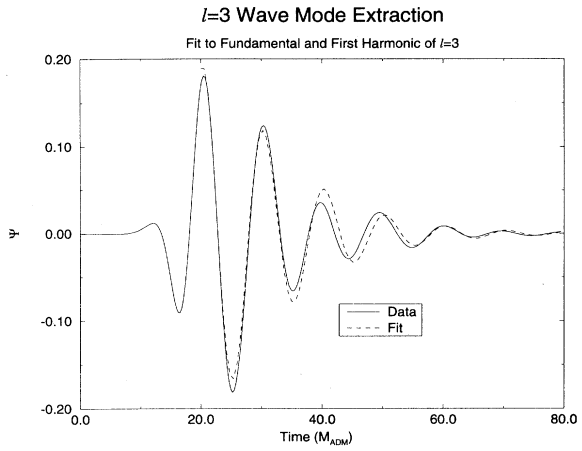

FIG. 25. This figure shows the numerically extracted $\ell = 3$ waveform and its fit to the two lowest $\ell = 3$ quasinormal modes for the run labeled $r4$.

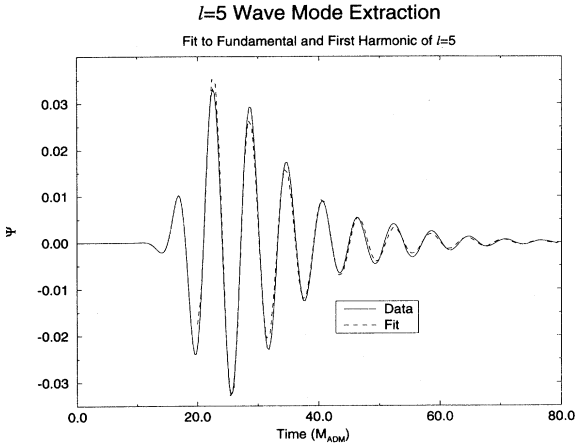

FIG. 27. This figure shows the numerically extracted $\ell = 5$ waveform and its fit to the two lowest $\ell = 5$ quasinormal modes for the run labeled $r4$.

case of the even-parity radiation we include a constant offset in the fit to account for the nonsphericity of the spacetime. The fit is good in all cases.

The calculation $r4$ is the second fastest rotator in this series. This rotation parameter ($a/m = 0.7$) was attained by reducing the strength of the Brill wave rather than by increasing the value of the angular momentum, and it is thus a different construction from runs $r0$ to $r3$. Large positive-amplitude Brill waves make it difficult to create spacetimes with large values of a/m, as they increase the mass significantly. We show the plots for the radiation in the $\ell = 2$, 3, 4, and 5 modes for this run in Figs. 24, 25, 26, and 27, respectively. In each case we fit the wave function to the fundamental and first harmonic mode for the appropriate value of ℓ. Again, the fit is good in all cases.

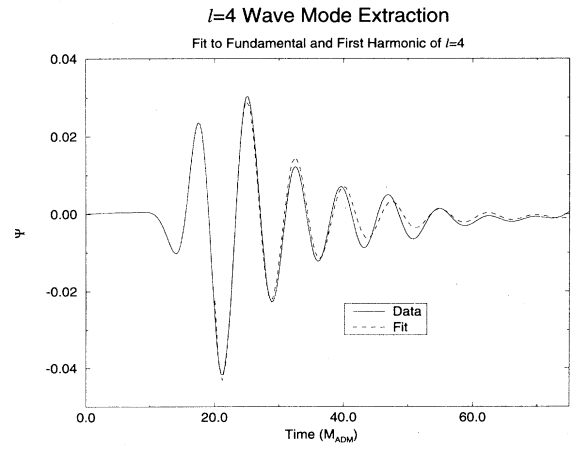

FIG. 26. This figure shows the numerically extracted $\ell = 4$ waveform and its fit to the two lowest $\ell = 4$ quasinormal modes for the run labeled $r4$.

The run labeled $r5$ is a special case. No "Brill wave" distortion is present in the spacetime except the distortion necessary to make the hole conformally flat. Both the three-metric and the extrinsic curvature are given by the simple solution of Bowen and York: $H_E = 3J\Psi^{-6}$ and $H_F = 0$. Bowen-York black holes are tricky to evolve, because they are so close to the Kerr black hole, yet this is the only method by which we have obtained a hole that rotates so rapidly. The presence of a Brill wave both stabilizes the spacetime and reduces the rotation parameter.

We note that in all these spacetimes, as the rotation is increased, an ever smaller fraction of the energy available as radiation is able to escape from the black hole. The dominant energy source in this problem is the imposed gravitational wave at $\eta = 1.0$. Because of our coordinate transformation, a constant η value maps to an ever decreasing value of r as a/m approaches unity, and the width of the packet in the η direction is effectively decreasing as a/m is increased; therefore, less energy is distributed in the region outside the horizon.

We note that in all these spacetimes it is approximately true that $M_{\rm rad} + M_{\rm AH,final}$ is equal to $M_{\rm ADM}$. The "final" apparent horizon mass is, however, really the mass as given around $(30\text{–}40)M$, since after that time large gradients in the radial metric variable A make it difficult to accurately obtain the horizon and bring about the well-known artificial inflation of the hole's mass at late times.

VI. CONCLUSIONS AND FUTURE WORK

Rotating vacuum black hole spacetimes are a significantly more complex type of axisymmetric vacuum spacetime than their nonrotating counterparts. In this paper we have applied a new code, designed to evolve rotating black holes, to evolve a new family of rotating black hole initial data sets. We developed a series of tools to

analyze these spacetimes, including even- and odd-parity waveform extraction and various techniques to study the apparent horizons of these spacetimes. We showed that measurements of the horizon can be used to determine the mass, angular momentum, and oscillation frequency of the black holes. Distorted rotating holes are shown to oscillate about their stationary "Kerr" equilibrium configurations.

Studies of a new class of odd-parity distorted nonrotating black holes were also made, and the waveforms and horizons were analyzed in detail. In all cases the normal modes of the black holes were shown to be excited and dominate the wave forms. We also determined, for the first time, the $\ell = 5$ quasinormal modes of a black hole by direct measurement of our numerically evolved spacetimes which were later verified by black hole perturbation theory techniques by Leaver. Finally, we were able to determine the final mass of the black hole by measuring the horizon area and compared it to the total ADM mass of the spacetime. The difference between these measurements agreed with the total energy radiated to within a few percent, showing the high degree of accuracy we are able to obtain in these studies.

There is more work to be done in this for which our code will be useful. We plan to discuss, in future papers, other features of the initial data sets and to look at new data sets. We plan to study spacetimes with "cosmic-screw"-type symmetry, which allows for rotation with equal and opposite amounts above and below the equatorial plane. Ultimately, we plan to study the collision of rotating black holes.

ACKNOWLEDGMENTS

We would like to thank Andrew Abrahams, Pete Anninos, David Bernstein, Larry Bretthorst, Karen Camarda, Greg Cook, David Drabold, David Hobill, Peter Leppik, Larry Smarr, and Wai-Mo Suen for many helpful suggestions throughout the course of this work. We are also especially grateful to Edward Leaver for computing the $\ell = 5$ quasinormal modes of black holes so that we could compare them to our results. This work was supported by NCSA, and by Grants Nos. NSF PHY94-07882 and ASC/PHY93-18152 (ARPA supplemented). The calculations were performed at NCSA on the Cray Y-MP and at the Pittsburgh Supercomputing Center on the Cray C-90. Unpublished and future related work may be accessed through our webserver at http://jean-luc.ncsa.uinc.edu. Symbolic manipulations were performed using MathTensor and Mathematica.

[1] D. Bernstein, D. Hobill, E. Seidel, L. Smarr, and J. Towns, Phys. Rev. D **50**, 5000 (1994).
[2] D. Bernstein, D. Hobill, E. Seidel, and L. Smarr, Phys. Rev. D **50**, 3760 (1994).
[3] A. Abrahams, D. Bernstein, D. Hobill, E. Seidel, and L. Smarr, Phys. Rev. D **45**, 3544 (1992).
[4] P. Anninos, D. Bernstein, D. Hobill, E. Seidel, L. Smarr, and J. Towns, in *Computational Astrophysics: Gas Dynamics and Particle Methods*, edited by W. Benz, J. Barnes, E. Muller, and M. Norman (Springer-Verlag, New York, in press).
[5] S. Brandt and E. Seidel, preceding paper, Phys. Rev. D **52**, 856 (1995).
[6] S. Brandt and E. Seidel (unpublished).
[7] J. Bowen and J. W. York, Phys. Rev. D **21**, 2047 (1980).
[8] D. Bernstein, Ph.D. thesis, University of Illinois Urbana-Champaign, 1993.
[9] P. Anninos, D. Bernstein, S. Brandt, D. Hobill, E. Seidel, and L. Smarr, Phys. Rev. D **50**, 3801 (1994).
[10] S. W. Hawking and G. F. R. Ellis, *The Large Scale Structure of Spacetime* (Cambridge University Press, Cambridge, England, 1973).
[11] P. Anninos, D. Bernstein, S. Brandt, J. Libson, J. Massó, E. Seidel, L. Smarr, W.-M. Suen, and P. Walker, Phys. Rev. Lett. **74**, 630 (1995).
[12] J. York, in *Frontiers in Numerical Relativity*, edited by C. Evans, L. Finn, and D. Hobill (Cambridge University Press, Cambridge, England, 1989).
[13] D. Christodoulou, Phys. Rev. Lett. **25**, 1596 (1970).
[14] Note that if $J/M_{\rm ir}^2 > 2$, then as the horizon area increases $M_{\rm AH}$ will actually decrease. However, no Kerr solution has this perverse value of $J/M_{\rm ir}^2$, and the final solution we evolve towards must be a Kerr solution. In an axisymmetric spacetime this means, therefore, that during the subsequent evolution the hole's area must increase until it is at least $M_{\rm AH} = \sqrt{J}$. This extreme case does not occur in any spacetime considered here.
[15] J. Massó, E. Seidel, W.-M. Suen, and P. Walker (unpublished).
[16] L. L. Smarr, Phys. Rev. D **7**, 289 (1973).
[17] E. Seidel and W.-M. Suen, Phys. Rev. Lett. **69**, 1845 (1992).
[18] A. Abrahams and C. Evans, Phys. Rev. D **42**, 2585 (1990).
[19] V. Moncrief, Ann. Phys. (N.Y.) **88**, 323 (1974).
[20] T. Regge and J. Wheeler, Phys. Rev. **108**, 1063 (1957).
[21] C. T. Cunningham, R. H. Price, and V. Moncrief, Astrophys. J. **224**, 643 (1978).
[22] G. L. Bretthorst, *Bayesian Spectrum Analysis and Parameter Estimation* (Springer-Verlag, New York, 1988).
[23] E. W. Leaver, Proc. R. Soc. London **A402**, 285 (1986).
[24] A. Abrahams and C. Evans, Phys. Rev. D **46**, R4117 (1992).
[25] M. C. Miller and F. K. Lamb, Astrophys. J. **439**, 828 (1994).
[26] E. Seidel and S. Iyer, Phys. Rev. D **41**, 374 (1990).

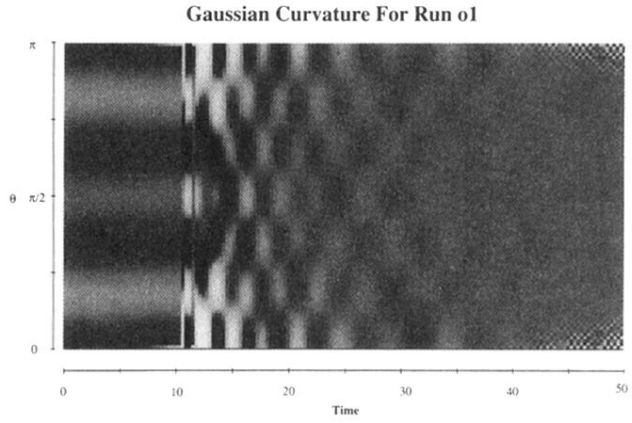

FIG. 5. We show the horizon history diagram for the run labeled *o*1. The Gaussian curvature κ is mapped to a gray scale on the surface of the horizon. The vertical axis gives the angular location on the horizon, and the horizontal axis traces out the time development. As discussed in the text, we see a pattern that repeats at twice the $\ell = 3$ QNM frequency in accordance with theoretical expectations. In the figure, dark regions are more highly curved than light regions.

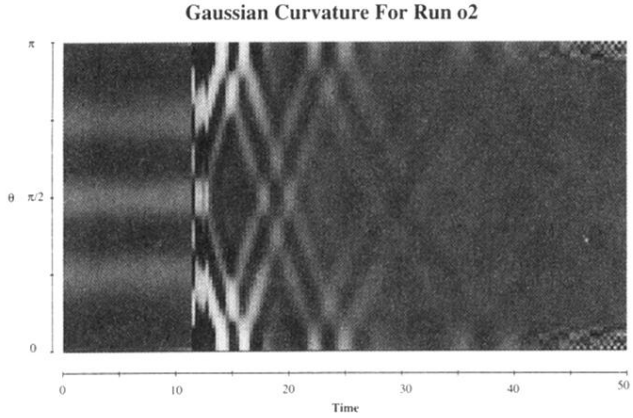

FIG. 6. In this plot we show the horizon history diagram for the run labeled $o2$. Hence the Gaussian curvature shows a diamond pattern, a result of the mixing of several frequencies of the $\ell = 3$ and $\ell = 5$ quasinormal modes. In the figure, dark regions are more highly curved than light regions. See text for details.